

Single-mode air-clad liquid-core waveguides on a surface energy patterned substrate

Stijn Vandewiele,^{1,2,3,*} Toon Brans,^{1,3} Liesbet Van Landschoot,^{2,3} Katarzyna Komorowska,^{2,3} Steven Verstuyft,^{2,3} Ananth Subramanian,^{2,3} Chen Hu,^{2,3} Filip Beunis,^{1,3} and Roel Baets^{2,3}

¹Liquid Crystals and Photonics Group, Department of Electronics and Information Systems, Ghent University, 41 Sint-Pietersnieuwstraat, Ghent 9000, Belgium

²Photonics Research Group, Department of Information Technology, Ghent University, 41 Sint-Pietersnieuwstraat, Ghent 9000, Belgium

³Center for Nano- and Biophotonics (NB-Photonics), Ghent University, 41 Sint-Pietersnieuwstraat, Ghent 9000, Belgium

*Corresponding author: stijn.vandewiele@ugent.be

Received May 1, 2014; revised June 12, 2014; accepted June 29, 2014;
posted July 17, 2014 (Doc. ID 210699); published August 15, 2014

We demonstrate a new kind of single-mode micro-optical waveguide based on a liquid core on top of solid substrate and air cladding. The liquid is held in place by surface tension and patterned surface energy on the substrate. Due to the smooth nature of the liquid/air interface down to the molecular level, low scattering losses are expected. Losses were measured to be -6.0 and -7.8 dB/cm for, respectively, 12 and 9 μm wide waveguides. © 2014 Optical Society of America

OCIS codes: (230.7370) Waveguides; (130.3130) Integrated optics materials; (310.2790) Guided waves; (220.4000) Microstructure fabrication.

<http://dx.doi.org/10.1364/OL.39.004942>

Optofluidics is an emerging field aimed at incorporating functionalities offered by photonics together with microfluidics into one device. By exploiting the benefits from this “marriage of optics and fluidics” [1], novel functionalities can be realized. As discussed in recent reviews [1–3], this field has already resulted in numerous applications including the electrowetting lens [4], optical switches [5–7], on-chip light generation [8], dye lasers [9], and lab-on-chip sensing [3].

Different platforms for planar optofluidics have been developed. They all strive toward attaining high modal overlap of the optical field with the liquid, as this increases the tuning and sensing sensitivity [10]. In this respect, liquid core waveguides are particularly promising.

The main challenge in the creation of a planar liquid core waveguide resides in the fabrication of a device with a substrate and cladding that have a lower refractive index than the fluidic core. Different solutions have been proposed for this, such as a liquid cladding/liquid core waveguide design [11] and a liquid core/air cladding waveguide with increased modal overlap [8]. Another strategy is followed by using hollow core anti-resonant reflecting optical waveguides (ARROW) [10,12], which rely on diffraction instead of refraction for the confinement of light. All of these solutions not only allow simultaneous guiding of light and material but also light switching and measurements of refractive index changes.

A novel kind of liquid core/air cladding micro-optical waveguide was recently demonstrated in [13]. This kind of waveguide is confined on top of a substrate by a local change in surface energy. As is known from the Young–Dupré equation [14], the contact angle θ of liquid on a planar surface in plain air is determined by the surface energy (γ) balance among the solid–vapor (SV), solid–liquid (SL), and liquid–vapor (LV) interfaces:

$$\gamma_{SV} - \gamma_{SL} - \gamma_{LV} \cos(\theta) = 0. \quad (1)$$

The contact angle θ and waveguide width are important parameters in defining the final shape of the waveguides.

In liquid droplets, the surface morphology is determined by the well-known Young–Laplace equation [15]:

$$\Delta P_0 + \Delta \rho g h = \gamma_{LV} \left(\frac{1}{R_1} + \frac{1}{R_2} \right), \quad (2)$$

with ΔP_0 the pressure difference at a reference plane of the LV interface, the hydrostatic force $\Delta \rho g h$, and $R_{1,2}$ the principal radii of curvature. However, for structures smaller than the capillary length $l_c = \sqrt{\gamma_{LV}/g|\Delta \rho|}$, bulk forces can be neglected, and the morphology of the liquid is only governed by the surface and line forces.

In this Letter, we demonstrate for the first time a single-mode liquid core/air cladding micro-optical waveguide. To confine the liquid on a plane surface, we alter the surface energy locally in rectangular stripes of a low γ_{SL} in a high γ_{SL} environment as demonstrated before in [16]. The solid/liquid/vapor interface of an applied droplet will then be pinned to the surface energy border as described by Lipowsky *et al.* [17]. θ varies between that of the low γ_{SL} and high γ_{SL} regions as determined by Eq. (1), depending on the liquid volume.

The liquid waveguides will thus have the shape of capped cylindrical threads fully determined by their width and contact angle θ . The influence of these parameters on the optical properties, such as the modal index and confinement factor, were simulated in COMSOL. We performed the simulations for the oil SL 5267 (Santolubes SL 5267, refractive index $n = 1.63$ at $\lambda = 1550$ nm and capillary length $l_c = 206$ μm) on glass substrate (SCHOTT Borofloat 33, refractive index $n = 1.46$ at $\lambda = 1550$ nm). Simulations show a single-mode region for a contact angle between 10.1° and 16.4° when the width is 9.2 μm . Figure 1 shows the electric field amplitude $|E|$ of a single-mode waveguide with $\theta = 14.0^\circ$ and width = 9.2 μm . The simulated confinement factor is 52.80% in this case, while 43.48% and 3.72% of the optical power resides in the substrate and air cladding, respectively.

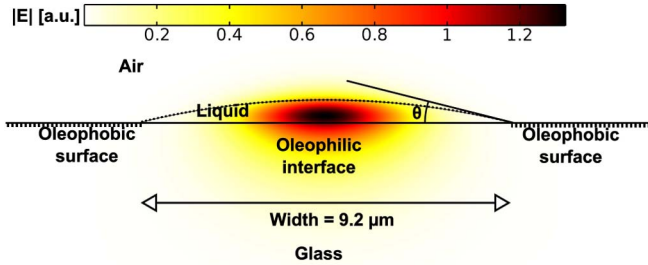


Fig. 1. Simulation of the electric field amplitude $|E|$ of a single-mode waveguide with contact angle $\theta = 14.0^\circ$ and width = $9.2 \mu\text{m}$.

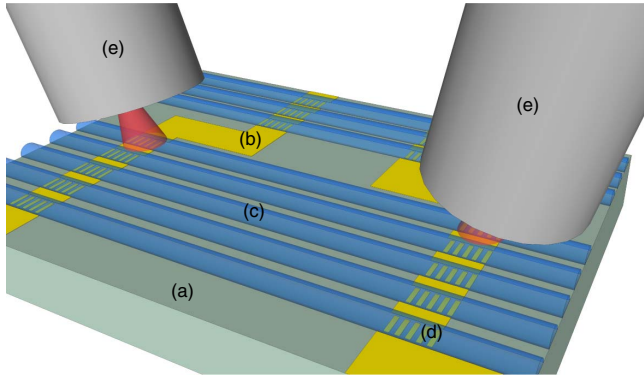


Fig. 2. Conceptual representation of the liquid waveguides with grating couplers to couple in and out the guided light. (a) Glass substrate. (b) Gold interconnecting paths necessary in the grating fabrication step. (c) Liquid waveguides. (d) Grating couplers. (e) Optical fibers that launch and capture coupled light.

We fabricated the proof-of-principle device through three distinctive steps. The resulting device is shown in Figs. 2 and 3.

For the first step, gold strips [Fig. 2(b)], in which gratings [Fig. 2(d)] are etched, are created on the glass substrate. To allow loss measurements, two gratings per waveguide are present, and the gold strips and gratings are spaced at different distances. These gold strips are produced by means of standard lithography, sputtering of titanium as an adhesion layer between the glass substrate and gold layer, evaporation of gold, and a lift-off process. Next a focused ion beam is used to etch gratings

in these strips. To suppress charging and drifting effects, the interconnected gold strips are electrically grounded.

The resulting fabricated gold strips are $25 \mu\text{m}$ wide and spaced at four different distances (0.6 , 5.0 , 10.0 , and 15.0 nm) center to center. SEM images of the cross section showed that the gratings have a thickness of 48 nm ($10 \text{ nm Ti}/38 \text{ nm Au}$), while a top view (Fig. 3) shows a period of $1.27 \mu\text{m}$ and a fill factor of ± 0.4 .

In the second fabrication step, the surface energy is changed locally. By spin-coating an adhesion promoter (TI prime, MicroChemicals) on the glass substrate, the surface is rendered oleophilic. Next, a lithographic pattern is created, and the antiadhesion regions (low surface energy γ_{SV}) are made by deposition of (tridecafluoro-1,1,2,2-tetrahydrooctyl)trimethoxysilane, a self-assembly molecule (SAM) well known from nanoimprint processing techniques [18]. The creation of this antiadhesion layer is realized by deposition of the molecules from the vapor phase at room temperature. After a curing step of 15 min at 120°C , the photoresist is removed in a lift-off process using dimethyl sulfoxide at 80°C . The resulting surface roughness was measured with an atomic force microscope and shows that $R_a = 1.8$ and 1.5 nm for the oleophilic and antiadhesion regions, respectively.

The change in surface energy for glass coated with an oleophilic or ambiphobic layer was investigated by measuring the change in contact angle for SL 5267 oil when applied on a coated glass substrate. Measurements, using a self-built contact angle measurement setup combined with publicly available analysis software [15], show that for the oleophilic region θ decreases from 17° to less than 5° . This is well below $\arccos(\pi/4) \approx 38^\circ$, which is necessary to obtain stable threads [17]. On the high-surface-energy γ_{SL} area, θ increases to $74 \pm 8^\circ$ due to the PTFE-like structure of the antiadhesion layer.

In the final fabrication step, the liquid is deposited by a dip coating process. Two fabricated samples are shown in Figs. 3(b) and 3(c). Liquid filaments with a design width down to $1.5 \mu\text{m}$ and up to $12.0 \mu\text{m}$ were successfully fabricated. As shown in Fig. 3(c), it is possible to create bent waveguides. The waveguides take on the pattern of the oleophilic region without any ripples along the surface energy border. Although the volume of the liquid filaments is small ($\approx 0.1 - 1 \text{ nl}/\mu\text{m}$) and the surface area is high ($\approx 10 \mu\text{m}^2/\mu\text{m}$), no significant evaporation was

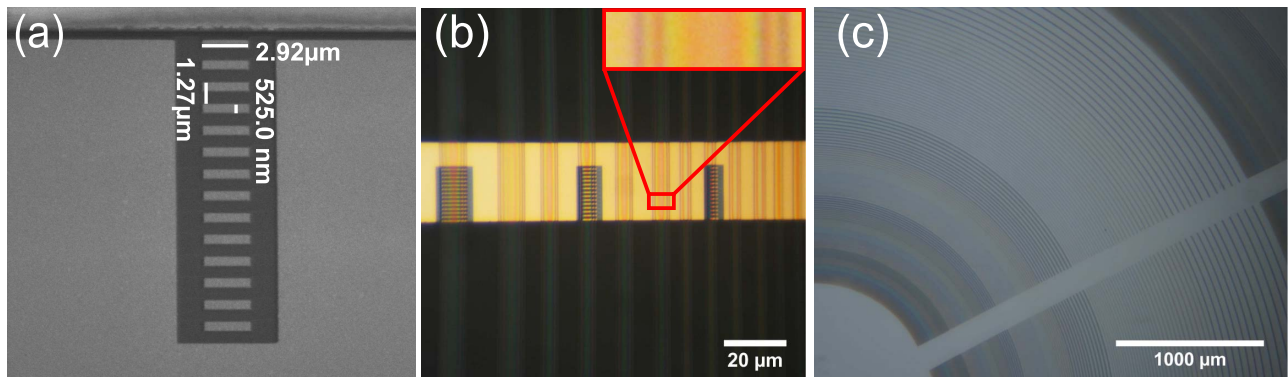


Fig. 3. (a) SEM image of a gold grating coupler on glass. (b) Fabricated device with grating couplers and an inset showing a thin-film interference pattern for a single waveguide. (c) Demonstration of bent waveguides.

Table 1. Measured Contact Angles and Widths of Waveguides Used During Optical Measurements with Gratings^a

| | Wg1 | Wg2 | Wg3 | Wg4 | Wg5 | Wg6 |
|--|-------|-------|------|-------|-------|------|
| Length [mm] | 0.6 | 0.6 | 0.6 | 5.0 | 5.0 | 5.0 |
| Measured width [$\pm 0.1 \mu\text{m}$] | 12.2 | 9.2 | 6.2 | 12.5 | 9.3 | 6.3 |
| Best fit contact angle [$^\circ$] | 15.0 | 14.0 | 13.7 | 15.2 | 13.6 | 13.7 |
| — | — | — | — | — | — | — |
| No. propagating TE modes | 3 | 1 | 0 | 4 | 1 | 0 |
| Confinement factor [%] | 75.79 | 52.80 | — | 77.54 | 51.32 | — |
| Modal overlap with substrate [%] | 21.50 | 43.48 | — | 19.89 | 44.95 | — |

^aThese parameters were used to simulate confinement factor and modal overlap with the glass substrate, given here for the fundamental quasi-TE mode only.

observed. The waveguides showed to be stable over a period of 18 months when enclosed in a sample box.

To verify the width of the waveguides, the sample was put under a microscope in reflection mode with a $100\times$ objective and a halogen light source. As shown in Table 1, these agree well with the designed widths of 6.0, 9.0, and $12.0 \mu\text{m}$. The exact cross-sectional profile of straight liquid filaments was measured by capturing an image of the filaments with the same microscope equipped with a bandpass light filter ($\lambda = 450\text{--}490 \text{ nm}$). As can be seen in Fig. 3(b), a thin-film interference pattern is visible on the liquid filaments due to the interference of reflected light on the air–liquid and liquid–glass interfaces. This light reflection can be modeled based on localized thin-film interference neglecting the curvature of the liquid, while the liquid profile has a circular cap cross section. From the waveguide width, the refractive index of the materials, and the position and number of intensity maxima (or minima), it is then possible to measure the contact angle and height of the liquid using this model combined with a least-squares fitting method.

We observe different contact angles for the waveguides, depending on their position on the substrate. We believe this is due to a nonuniform fill factor of low-surface-energy γ_{SL} regions in a high-surface-energy γ_{SL} surrounding, affecting the film thickness in the dip coating process as described in [19]. Therefore, the exact optical mode profile in the waveguide and the coupling efficiency of the grating coupler may vary as well.

Loss measurements were performed by coupling light from an LED in and out of the waveguide through a fiber [Fig. 2(e)] making an angle of 15° with the surface normal. This angle of incidence was chosen to optimize the coupling efficiency between the grating coupler and the fiber [20]. The out-coupled power $P(\lambda)$ was measured with an optical spectrum analyzer for two waveguide lengths $L_1 = 600 \mu\text{m}$ and $L_2 = 5000 \mu\text{m}$. The propagation loss $\alpha_{\text{dB/cm}}(\lambda)$ is then given by

$$\alpha_{\text{dB/cm}}(\lambda) = \frac{P_2(\lambda) - P_1(\lambda)}{L_2 - L_1}. \quad (3)$$

Figure 4 shows the measured loss spectrum for design width = 6, 9, and $12 \mu\text{m}$. The $6 \mu\text{m}$ wide waveguides are clearly in cut-off mode, agreeing with mode analysis simulations in COMSOL, as shown in Table 1. The simulations for this width show that the effective propagation indices n_{eff} of the fundamental mode in quasi-TE

polarization at $\lambda = 1550 \text{ nm}$ are 1.458 and 1.457 for the 0.6 and 5.0 mm long waveguide, respectively. These values are lower than the refractive index of the glass substrate 1.460.

Simulations show that the $9 \mu\text{m}$ wide waveguides are single mode, while both $12 \mu\text{m}$ wide waveguides are multimode according to simulations. The grating-coupler efficiency was measured to be 2% (width = $9 \mu\text{m}$) and 5% (width = $12 \mu\text{m}$) at $\lambda = 1550 \text{ nm}$.

The propagation loss is -5.7 to -6.0 dB/cm and -7.6 to -7.8 dB/cm for design width = 12 and $9 \mu\text{m}$, respectively. These values are considerably lower than those previously obtained for free-standing optofluidic waveguides [13]. The specification sheets denote a loss of liquid and glass at 1550 nm of -0.3 and -1.58 dB/cm , respectively. Hence, the measured loss is higher than expected purely on the basis of material absorption. This may be ascribed to different reasons. First, a propagation length of 0.6 mm may not be enough to ensure that all higher-order evanescent modes are extinct and only the fundamental mode is guided. These higher-order modes may then couple out, augmenting the output power for short waveguides. Second, variations in width, contact angle, and grating coupler fabrication may result in different grating coupler efficiencies for each loss measurement, while Eq. (3) is only valid for constant coupling efficiency.

Another noteworthy behavior is the parasitic Fabry–Perot etalon, manifesting as a ripple on the loss measurement with a free spectral range of $\pm 13 \text{ nm}$. We believe the Fabry–Perot etalon is formed by reflections at the top and bottom of the glass substrate.

We have demonstrated that it is possible to create oily liquid micro-optical waveguides on a glass substrate by patterning the surface energy. Loss measurements showed lower losses than previously reported. These values are still higher than expected, for which different

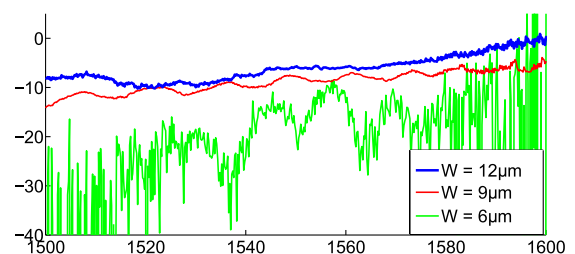


Fig. 4. Measured loss in dB/cm for the three waveguide design widths W . A parasitic Fabry–Perot etalon is clearly visible.

possible explanations were given. The waveguides take on the shape of the oleophilic regions without any visible ripples along the surface energy border. This resulted in various waveguides having widths spanning from 6 to 12 μm , which show the cut-off, single-mode, and multi-mode operation at a wavelength of 1550 nm, confirmed through mode analysis simulations. Besides straight waveguides, we have demonstrated it is possible to fabricate bent waveguides. Additionally, the waveguides are stable over a period of several months. In future work, we will investigate the feasibility of this material platform for resonators with a high Q factor.

This research was supported by the IAP-VI project photon@be funded by BELSPO, the Belgian Science Policy program, and the Hercules Foundation (project no. AUGE/013). The authors would like to thank P. Pirasteh-Charrier for her help with the fabrication of the grating couplers.

References

1. H. Schmidt and A. Hawkins, *Nat. Photonics* **5**, 598 (2011).
2. D. Psaltis, S. R. Quake, and C. Yang, *Nature* **442**, 381 (2006).
3. X. Fan and I. M. White, *Nat. Photonics* **5**, 591 (2011).
4. L. Dong, A. K. Agarwal, D. J. Beebe, and H. Jiang, *Nature* **442**, 551 (2006).
5. J.-M. Lim, J. P. Urbanski, T. Thorsen, and S.-M. Yang, *Appl. Phys. Lett.* **98**, 044101 (2011).
6. K. Campbell, A. Groisman, U. Levy, L. Pang, S. Mookherjea, D. Psaltis, and Y. Fainman, *Appl. Phys. Lett.* **85**, 6119 (2004).
7. J. Uebbing, S. Hengstler, D. Schroeder, S. Venkatesh, and R. Haven, *J. Microelectromech. Syst.* **15**, 1528 (2006).
8. J.-M. Lim, S.-H. Kim, J.-H. Choi, and S.-M. Yang, *Lab Chip* **8**, 1580 (2008).
9. Z. Li and D. Psaltis, *Microfluid. Nanofluid.* **4**, 145 (2008).
10. H. Schmidt and A. Hawkins, *Microfluid. Nanofluid.* **4**, 3 (2008).
11. D. Wolfe, R. Conroy, P. Garstecki, B. Mayers, M. Fischbach, K. Paul, M. Prentiss, and G. Whitesides, *Proc. Natl. Acad. Sci. USA* **101**, 12434 (2004).
12. D. Yin, H. Schmidt, J. P. Barber, E. J. Lunt, and A. R. Hawkins, *Opt. Express* **13**, 10564 (2005).
13. A. Jonáš, B. Yalizay, S. Akturk, and A. Kiraz, *Appl. Phys. Lett.* **104**, 091123 (2014).
14. P. G. de Gennes, *Rev. Mod. Phys.* **57**, 827 (1985).
15. A. Stalder, T. Melchior, M. Müller, D. Sage, T. Blu, and M. Unser, *Colloids Surf. A* **364**, 72 (2010).
16. H. Gau, S. Herminghaus, P. Lenz, and R. Lipowsky, *Science* **283**, 46 (1999).
17. R. Lipowsky, M. Brinkmann, R. Dimova, C. Haluska, J. Kierfeld, and J. Shillcock, *J. Phys. Condens. Matter* **17**, S2885 (2005).
18. G. Jung, Z. Li, W. Wu, Y. Chen, D. Olynick, S. Wang, W. Tong, and R. Williams, *Langmuir* **21**, 1158 (2005).
19. A. Darhuber, S. Troian, J. Davis, S. Miller, and S. Wagner, *J. Appl. Phys.* **88**, 5119 (2000).
20. G. Roelkens and D. Thourhout, *Silicon Photonics II*, D. J. Lockwood and L. Pavesi, eds., Vol. 119 of *Topics in Applied Physics* (Springer, 2011), p. 71.